



ELSEVIER

Contents lists available at ScienceDirect

Journal of Magnetism and Magnetic Materials

journal homepage: www.elsevier.com/locate/jmmmMagnetic and thermoelectric properties of three different atomic ratio of Bi/Mn in BiMn₂O₅: DFT approachWilayat Khan^{a,*}, A.H. Reshak^{a,b}, Khairul Rafezi Ahmad^b, Z.A. Alahmed^c^a New Technologies-Research Centre, University of West Bohemia, Univerzitni 8, 306 14 Pilsen, Czech Republic^b Center of Excellence Geopolymer and Green Technology, School of Material Engineering, University Malaysia Perlis, 01007 Kangar, Perlis, Malaysia^c Department of Physics and Astronomy, King Saud University, Riyadh 11451, Saudi Arabia

ARTICLE INFO

Article history:

Received 9 November 2013

Received in revised form

5 June 2014

Available online 24 June 2014

Keywords:

Electronic structure

Magnetic properties

Thermoelectric properties

Boltztrap code

DFT

ABSTRACT

Electronic structure and magnetic properties of the three different samples of BiMn₂O₅, are calculated using the density functional theory (DFT). These samples have different Bi/Mn concentration. For simplicity, we suggest to call them as A, B and C. The calculated band structures show half metallicity for all samples, and possess 100% spin polarization at the Fermi level. The spin up/down density of states are calculated using Engel-Vosko generalized gradient approximation (EV-GGA). We have discussed the effect of Mn magnetic moment (μ_B) on the electronic and magnetic properties of the entire samples. The temperature dependent thermoelectric properties like electrical and thermal conductivity, Seebeck coefficient and power factor are also calculated, employing the Boltzmann transport theory under the BoltzTraP code. Our results indicated that these properties are strongly dependent on Bi/Mn concentration.

© 2014 Elsevier B.V. All rights reserved.

1. Introduction

The smart materials are very sensitive to the external stimuli such as temperature, stress and the magnetic fields or electric fields. Some other technological inputs are thus expected. The multiferroic materials fit in to these types of smart materials when their ferroelectric properties can be seen by applying a magnetic field, prompting that an effective magnetoelectric coupling is present [1].

In recent years, two newly classes of multiferroic compounds have been come out in which ferroelectricity can be generated by either magnetic ordering [2] or charge ordering [3]. Marvelous work is dedicated to these novel categories of components, and isostructural RMn₂O₅ (R = uncommon earth, Y or Bi) insulators [4] are archetypal examples. In 1960s, Quezel-Ambrunaz et al. [5] and Bertaut et al. [6] were first time stated the RMn₂O₆ oxides following the single crystal growth by a Bi₂O₅ flux method. Subsequent on, the RMn₂O₅ class of components were identified to be basically applicable to a charge-ordering phenomenon in relation to the reality of two crystallographically independent sites for Mn atoms [7]. The suggested crystallographic structure is constructed up of [Mn⁴⁺O₆] octahedra sharing edges, which forms the infinite linear series along the *c* axis, and consistent with [Mn³⁺O₅] rectangle pyramids. Intending to induce innovative

physical properties, B-site substitution of RMn₂O₅ by Fe was conveyed out [8]. For the substitution ratio Mn/Fe = 1, high-resolution neutron powder X-ray diffraction (XRD) suggested that Fe³⁺ and Mn⁴⁺ ions were ordered in square-pyramidal and octahedral sites, respectively [9]. This proposed charge-ordering model is in comparison with preceding single-crystal XRD analysis in BiFeMnO material [10], where it was asserted that Fe³⁺ ions were only established on octahedral sites.

In the meantime, Nguyen and coworker depicted that the crystallographic phase of BiMn_{2-x}B_xO₅ (0 ≤ *x* ≤ 0.5; B = Fe, Al, and Ti) were steady even if the ratio of Mn³⁺ and Mn⁴⁺ was not equal to 1 with a minor boost of the cell parameters with *x* [11]. Considering the magnetic properties, BiMn₂O₅ exposes the magnetic structure in comparison with the inadequate magnetic structure observed for LnMn₂O₅ (Ln = lanthanide) [12]. Even if a magnetic transition from the paramagnetic-to-antiferromagnetic state was often observed when the temperature going to decrease, a low-temperature ferrimagnetic state has furthermore been exposed [13,14]. Certainly, more deviations are furthermore examined (i) on the transport properties when Alonso and co-workers [7] showed that their components were insulating with $\rho > 10^8 \Omega \text{ cm}$ at room temperature in contrast with Lin et al. [15] resulting that the high-temperature conductivity of their phase is thermally triggered ($E_A = 0.38 \text{ eV}$ inside the 200–450 K range) and (ii) on the dielectric response when Lin et al. [15] highlight resemblance between the activation energies obtained from the dielectric relaxation and that one which is obtained from the high temperature conductivity, to conclude that BiMn₂O₅ is

* Corresponding author. Tel.: +420 775 526 684.

E-mail address: [walayat76@gmail.com](mailto:walayyat76@gmail.com) (W. Khan).

not relaxer ferroelectric, contrary to the conclusion of Fier and co-workers [16]. Considering all of these research works, Liu et al. [17] aim to explain the magnetic and dielectric characteristics of BiMn_2O_5 , which depends on chemical compositions and/or the sintering phenomena used for preparation. Liu and co-researcher [17] proves the Bi deficiency by performing X-rays crystallographic study, and also explain the magnetic properties, specific heat, dielectric properties and multiferroic assets.

In the present theoretical work, our main aim is to study the spin polarized electronic structure and optical properties of three different samples of BiMn_2O_5 with different Bi/Mn concentration as we call them A, B and C, by using the full potential linearized augmented plane wave (FP-LAPW) in the frame work of WIEN2k computer package. In additional the thermoelectric properties namely, Seebeck coefficient, thermal and electrical conductivity and power factor are also calculated using the BoltzTraP code [18,19].

2. Computational method

We have carried out the self consistent calculations using the full-potential linear augmented plane-wave approach as implemented in the WIEN2k package [20]. This technique is widely experienced and is found to be the most accurate technique among the other techniques for executing electronic structure calculation of solids within density functional theory (DFT). The electronic exchange-correlation potentials are treated within the frame work of local density approximation (LDA) [21], generalized gradient approximation (GGA) [22] and Engel–Vosko generalized gradient approximation (EV – GGA) [23], which is far better than that of LDA. Despite considerable efforts in both experimental and theoretical studies [24], it should be pointed out that the previously reported result shows that both of LDA and GGA underestimated the energy gap. This is due to the fact that both LDA and GGA have simple forms and not sufficiently flexible to accurately reproduce both the exchange–correlation energy and its charge derivative [25]. To overcome this drawback we have used EVGGA, which goes beyond LDA and GGA.

In the FP – LAPW approach, the unit cell is divided into (I) non-overlapping atomic spheres (centered at the atomic sites) and (II) an interstitial region. The Muffin tin sphere radii are taken to be 2.20 a.u for Bi, 1.75a.u for Mn and 1.55a.u for O, for all samples (A, B and C) respectively. The equations used for the expansion of potential inside/outside the sphere are taken from Ref. [26]. We have used $G_{\text{max}} = 12$, which provide the accurate information about the plane wave cut-off. The self consistency is achieved by using 1000k points in the corresponding irreducible Brillion zone. The basis function is expanded by setting the R_{MT} (atomic sphere radii) time K_{max} (the interstitial plane wave cut-off) up to 7, which organized the size of the basis set. The recommended crystallographic symmetry is made up of $[\text{Mn}^{4+}\text{O}_6]$ octahedral sharing edges, which produces the infinite linear series along the c axis, and consistent with $[\text{Mn}^{3+}\text{O}_5]$ rectangle pyramids. The structure of the three samples of BiMn_2O_5 is orthorhombic with space group $Pbam(55)$. The crystal symmetry of BiMn_2O_5 is shown in Fig. 1. All atomic position for Bi, Mn and O atoms and the lattice constants of all three samples are given in Table 1. The inter-atomic distances between Mn–O and Bi–O atoms for the three samples, in comparison with the experimental data [17] are listed in Table 2.

All polycrystalline samples (A, B and C) of so-called composition BiMn_2O_5 were produced by a typical solid-state reaction technique start from the component Bi_2O_3 , Mn_2O_3 , and MnO_2 with purity above 99.9%. Liu et al. [17] have prepared the three samples of BiMn_2O_5 experimentally, according to the following precursor: (1) for the samples A and B: $\text{Bi}_2\text{O}_3 + \text{Mn}_2\text{O}_3 + 2\text{MnO}_2$ and (2) for the sample C: $\text{Bi}_2\text{O}_3 + 4\text{MnO}_2$. In these samples, Mn and

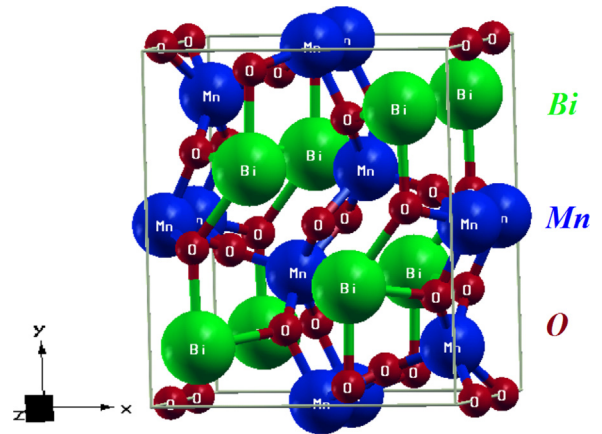


Fig. 1. Molecular structure of BiMn_2O_5 .

O occupancies are kept fixed, i.e. 2 Mn and 5 O atoms/formula unit and sequentially developed the occupancy of bismuth in alignment to judge the bismuth deficiency in assessment to ICP–OES investigation, the atomic ratio of Bi/Mn is 0.46 ± 0.01 for sample A, 0.48 ± 0.01 for sample B and 0.47 ± 0.01 for sample C [17].

3. Results and discussion

3.1. Electronic structure

In order to discuss the electronic structure of the three samples (A, B and C) in details, we have plotted the spin polarized band structures, as shown in Fig. 2(a)–(c). The spin-up band structure shows the metallic behavior (majority spin) and the spin-down band structure shows the semiconducting nature (minority spin) [27]. From Fig. 2, the three samples exhibit half metallic nature [17]. The formation of the band gap for the half metal compounds is due to the hybridization between Mn-d and Bi-d states. The band represented by red color (see Fig. 2(a)–(c)), is formed from the d states of Mn atom, which clearly crossing the Fermi level (E_F) in the majority spin polarization band structure, which exhibit the metallic nature in the three samples. The O-2p bands are situated below -3.5 eV, while the bands from E_F up to 3.5 eV are filled by Mn-3d. Conversely, in the minority spin polarization, there is a small gap which declared that the compounds are semiconductors having indirect band gap. The conduction band minimum (CBM) is situated at Z point of BZ, whereas the valence band maximum (VBM) is located between Z–X points of BZ. It is also noticed from Fig. 2 that the calculated band structure demonstrates that the electrons of these compounds are spin polarized at the Fermi level (E_F).

The total densities of states (TDOS) for the three samples (A, B and C) are shown in Fig. 3a. The TDOS near E_F shows the metallic tendency for majority spin and the semiconducting nature for minority spin orientation for all samples. It is clear from Fig. 3a, that the samples A and C exhibit similar structure, while in sample B the whole bands are shifted toward higher energy by around 0.1 eV, with respect to the band structure of samples A and C. The densities of states of the entire BiMn_2O_5 samples depend on the distinctiveness of the partially filled d-orbitals. Since the d-state of Mn atom occupied the states near E_F . Therefore, we have plotted the PDOS of the samples A, B and C for spin-up and spin-down, as shown in Fig. 3(b)–(d). From the spin-up/down PDOS, we have the capability to distinguish the angular momentum (l) of different symmetries.

The main contribution of the three samples to the PDOS appears from the d-state of Mn non-equivalent sites [28], (see

Table 1
Atomic positions for all samples (A, B, C).

Compound	Lattice constant			
Sample A	$a=7.5641^a, 7.5641^b$ (Å),		$b=8.5336^a, 8.5336^b$ (Å)	$c=5.7616^a, 5.7616^b$ (Å)
	Atomic position			
	Atom	X	Y	Z
	Bi	0.15949 ^a , 0.15885 ^b	0.16549 ^a , 0.16675 ^b	0.00000 ^a , 0.00000 ^b
	Mn(1)	0.00000 ^a , 0.00000 ^b	0.50000 ^a , 0.50000 ^b	0.2597 ^a , 0.2738 ^b
	Mn(2)	0.4067 ^a , 0.3846 ^b	0.3503 ^a , 0.3557 ^b	0.5000 ^a , 0.5000 ^b
	O(1)	0.00000 ^a , 0.00000 ^b	0.00000 ^a , 0.00000 ^b	0.2857 ^a , 0.2942 ^b
	O(2)	0.1527 ^a , 0.1484 ^b	0.4425 ^a , 0.4456 ^b	0.00000 ^a , 0.00000 ^b
	O(3)	0.1399 ^a , 0.1633 ^b	0.4244 ^a , 0.4194 ^b	0.5000 ^a , 0.5000 ^b
O(4)	0.3859 ^a , 0.3892 ^b	0.1970 ^a , 0.2046 ^b	0.2538 ^a , 0.2653 ^b	
Sample B	$a=7.5615^a, 7.5615^b$ (Å),		$b=8.5346^a, 8.5346^b$ (Å)	$c=5.7617^a, 5.7617^b$ (Å)
	Atomic position			
	Atom	X	Y	Z
	Bi	0.15932 ^a , 0.15905 ^b	0.16544 ^a , 0.16679 ^b	0.00000 ^a , 0.00000 ^b
	Mn(1)	0.00000 ^a , 0.00000 ^b	0.50000 ^a , 0.50000 ^b	0.2615 ^a , 0.2738 ^b
	Mn(2)	0.4065 ^a , 0.3850 ^b	0.3503 ^a , 0.3556 ^b	0.5000 ^a , 0.5000 ^b
	O(1)	0.00000 ^a , 0.00000 ^b	0.00000 ^a , 0.00000 ^b	0.2867 ^a , 0.2941 ^b
	O(2)	0.1493 ^a , 0.1480 ^b	0.4431 ^a , 0.4456 ^b	0.00000 ^a , 0.00000 ^b
	O(3)	0.1414 ^a , 0.1637 ^b	0.4238 ^a , 0.4192 ^b	0.5000 ^a , 0.5000 ^b
O(4)	0.3873 ^a , 0.3895 ^b	0.1985 ^a , 0.2046 ^b	0.2556 ^a , 0.2651 ^b	
Sample C	$a=7.5658^a, 7.5658^b$ (Å),		$b=8.5315^a, 8.5315^b$ (Å)	$c=5.7615^a, 5.7615^b$ (Å)
	Atomic position			
	Atom	X	Y	Z
	Bi	0.15951 ^a , 0.15913 ^b	0.16541 ^a , 0.16687 ^b	0.00000 ^a , 0.00000 ^b
	Mn(1)	0.00000 ^a , 0.00000 ^b	0.50000 ^a , 0.50000 ^b	0.2607 ^a , 0.2738 ^b
	Mn(2)	0.4067 ^a , 0.3848 ^b	0.3504 ^a , 0.3558 ^b	0.5000 ^a , 0.5000 ^b
	O(1)	0.00000 ^a , 0.00000 ^b	0.00000 ^a , 0.00000 ^b	0.2878 ^a , 0.2942 ^b
	O(2)	0.1499 ^a , 0.1481 ^b	0.4441 ^a , 0.4458 ^b	0.00000 ^a , 0.00000 ^b
	O(3)	0.1420 ^a , 0.1637 ^b	0.4252 ^a , 0.4197 ^b	0.5000 ^a , 0.5000 ^b
O(4)	0.3858 ^a , 0.3894 ^b	0.1982 ^a , 0.2047 ^b	0.2553 ^a , 0.2651 ^b	

^a Ref. [17].

^b Ref. This work.

Table 2
Bond length and bond angle for all samples (A, B, C).

Bond length (Å) (sample A)	Bond length (Å) (sample B)	Bond length (Å) (sample C)
Mn(1)–O(2)=1.953 ^a , 1.991 ^b	Mn(1)–O(2)=1.945 ^a , 1.990 ^b	Mn(1)–O(2)=1.942 ^a , 1.990 ^b
Mn(1)–O(3)=1.858 ^a , 1.923 ^b	Mn(1)–O(3)=1.859 ^a , 1.925 ^b	Mn(1)–O(3)=1.861 ^a , 1.924 ^b
Mn(1)–O(4)=1.890 ^a , 1.938 ^b	Mn(1)–O(4)=1.897 ^a , 1.937 ^b	Mn(1)–O(4)=1.898 ^a , 1.937 ^b
Mn(2)–O(1)=1.911 ^a , 1.919 ^b	Mn(2)–O(1)=1.902 ^a , 1.918 ^b	Mn(2)–O(1)=1.902 ^a , 1.918 ^b
Mn(2)–O(3)=2.114 ^a , 1.760 ^b	Mn(2)–O(3)=2.102 ^a , 1.760 ^b	Mn(2)–O(3)=2.102 ^a , 1.760 ^b
Mn(2)–O(4)=1.935 ^a , 1.869 ^b	Mn(2)–O(4)=1.923 ^a , 1.869 ^b	Mn(2)–O(4)=1.923 ^a , 1.869 ^b
Bi–O(1)=2.482 ^a , 2.519 ^b	Bi–O(1)=2.485 ^a , 2.519 ^b	Bi–O(1)=2.490 ^a , 2.520 ^b
Bi–O(2)=2.364 ^a , 2.381 ^b	Bi–O(2)=2.380 ^a , 2.381 ^b	Bi–O(2)=2.380 ^a , 2.381 ^b
Bi–O(2)=2.375 ^a , 2.384 ^b	Bi–O(2)=2.375 ^a , 2.386 ^b	Bi–O(2)=2.375 ^a , 2.384 ^b
Bi–O(4)=2.269 ^a , 2.341 ^b	Bi–O(4)=2.276 ^a , 2.340 ^b	Bi–O(4)=2.276 ^a , 2.340 ^b
Bi–O(4)=2.792 ^a , 2.775 ^b	Bi–O(4)=2.793 ^a , 2.773 ^b	Bi–O(4)=2.793 ^a , 2.774 ^b

^a Ref. [17].

^b Ref. This work.

Fig. 3(b)–(d)). The Mn-d states in A and C samples is non-localized in nature, this is attributed to the fact that the Mn-d states is positioned above E_F . It is obvious from Fig. 3(b)–(d), the Mn-d states of sample B exhibit larger shift toward higher energies in comparison to the other two samples in the spin-up PDOS. Whereas in spin-down PDOS the Mn-d states display a negligible shift with respect to samples A and C. The same behavior is also observed in the s/p-states of Mn atom, which depict small contribution to the PDOS, as shown in Fig. 3(b)–(d). The contribution of Mn to the PDOS can be compared to the afore-mentioned compounds. Bi-s/p states show strong contribution, while the contribution of O-s states in sample C is bigger than that for the other two samples as illustrated in Fig. 3(b)–(d). Following Fig. 3 (b)–(d), one can clarify that Bi-d/f states show negligible contribution to the PDOS. The s-states of the O atom exhibit negligible contribution as compared to p-states of O atom (Fig. 3(b)–(d)). Due

to the effect of the spin polarization all the spin-down states indicate a shift toward higher energy than spin-up states.

The density of states at E_F , ($N(E_F)$), is about 3.0 states/eV for the majority spin for all samples. This is due to the fact that the Mn-d state (delocalized state) in the majority spin strongly cuts E_F , as shown in Fig. 3(b)–(d), which exhibit 100% polarization at E_F . The calculated partial and total magnetic moments for the three samples (A, B, C) are listed in Table 3.

3.2. Optical properties

The expressions for complex dielectric function and its derivatives are mentioned elsewhere [29,30]. Since the investigated compounds are orthorhombic, therefore this symmetry allows only three non-zero components of the dielectric tensor namely $\epsilon^{xx}(\omega)$, $\epsilon^{yy}(\omega)$, and $\epsilon^{zz}(\omega)$. In Fig. 4(a) and (b), we have plotted the

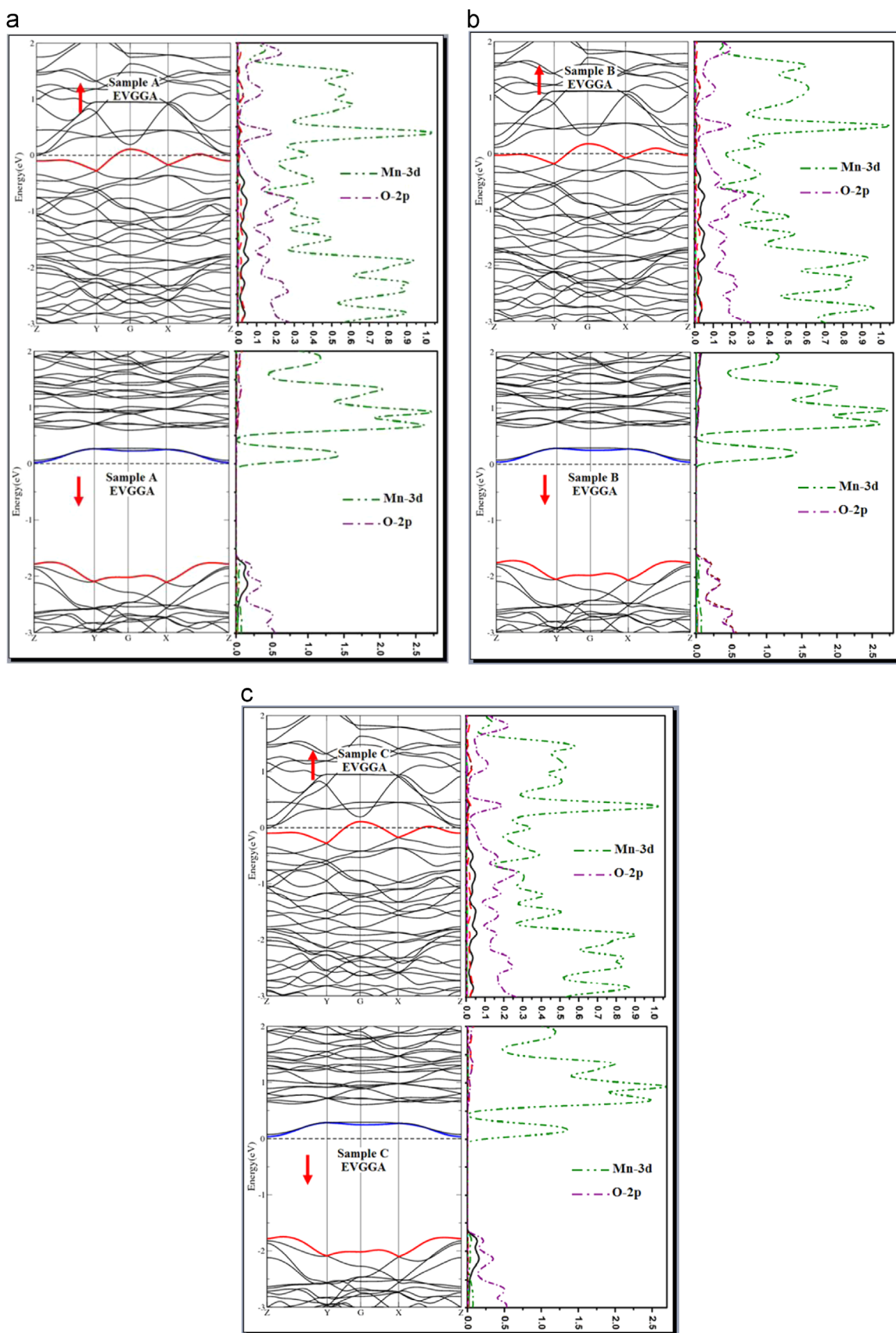


Fig. 2. Calculated band structures for spin-up/dn polarization of all samples (A, B, C), using EVGGA. (For interpretation of the references to color in this figure legend, the reader is referred to the web version of this article.)

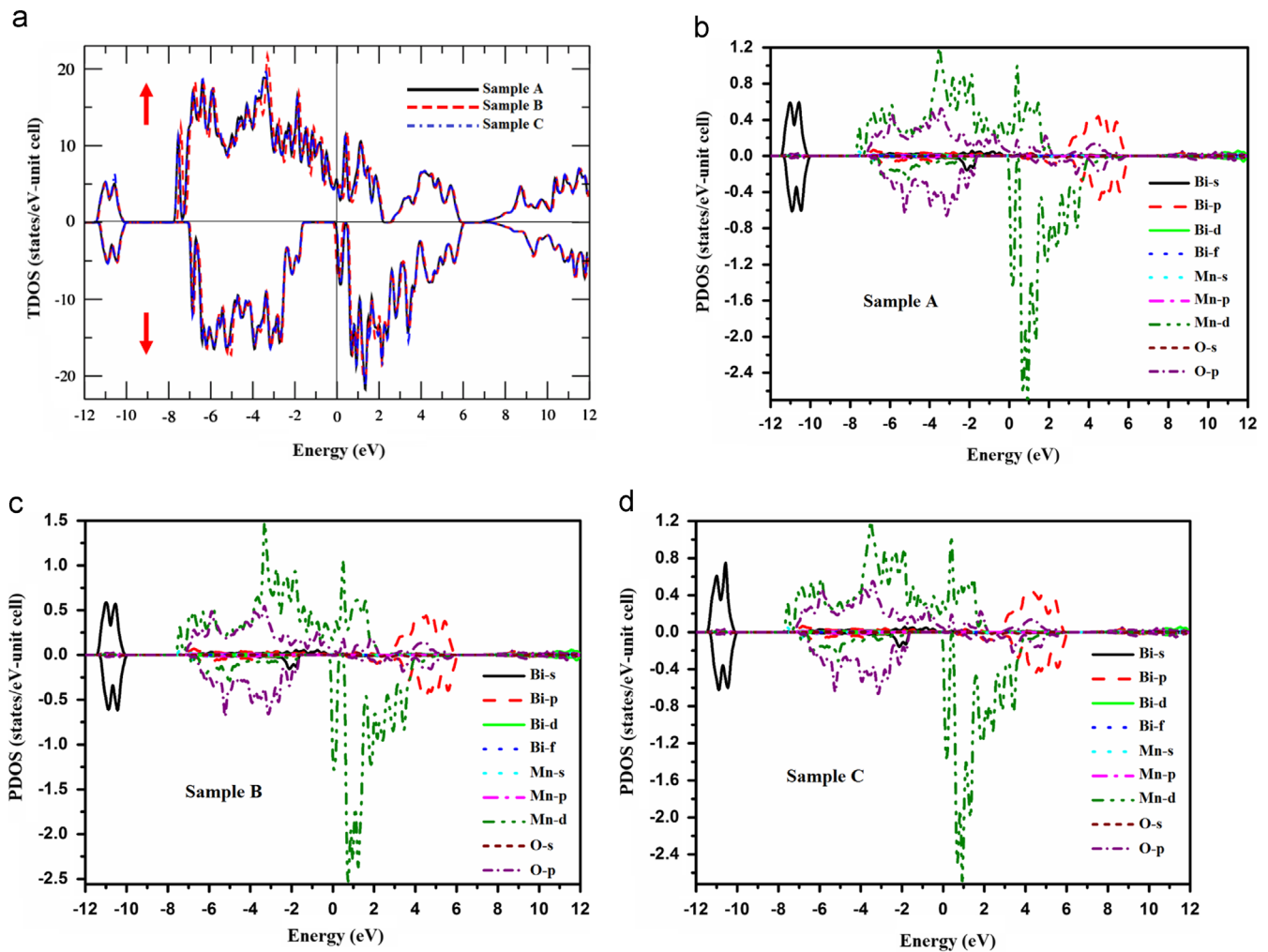


Fig. 3. Calculated total density state (TDOS) and partial density of states (PDOS) for spin-up/dn polarization of all samples (A, B, C), using EVGGA.

Table 3
Total and partial magnetic moments of all samples (A, B, C).

Total				Partial				
	Bi	Mn(1)	Mn(2)	O(1)	O(2)	O(3)	O(4)	
Magnetic moment μ_B								
Sample A	27.990	0.0316	3.0037	2.9728	0.0192	0.0370	0.0640	0.0297
Sample B	27.072	0.0309	2.8456	2.9454	0.0189	0.0280	0.0610	0.0292
Sample C	27.992	0.0318	3.0022	2.9719	0.0195	0.0373	0.0645	0.0298

average value of the frequency dependent imaginary part $\varepsilon_2^{ave}(\omega)$ [31] of the dielectric function for all the three samples. Fig. 4(a), shows the $\varepsilon_2^{ave}(\omega)$ for the spin-down of the three samples which show that there exist an optical gap, which supports our previous finding that the minority spin (spin-down) shows semiconducting nature. While Fig. 4(b) illustrates the $\varepsilon_2^{ave}(\omega)$ for the spin-up of the three samples. In spin-up polarization, there exists sharp rise around 1.0 eV for samples A and C, whereas it is at around 0.5 eV for sample B. This sharp rise is due to Drude term (intra-band transitions). This finding supports our previous finding that the majority spin (spin-up) exhibit metallic nature.

The spectra in Fig. 4(a) and (b) display several peaks, which lie in the energy range from 4.0 eV to 6.0 eV. On the other hand in spin-down polarization, $\varepsilon_2^{ave}(\omega)$ exhibits maximum peaks in the energy range from 3.0 eV to 7.5 eV, as illustrated in Fig. 4(a) and (b). We can

analyze the origin of peaks in the $\varepsilon_2^{ave}(\omega)$ spectra as follow; the spectral peaks at 7.55 eV for the samples A, B and C in Fig. 4a, and in Fig. 4b, the peaks at 6.5 eV for samples A and C and at 6.25 eV for sample B arise due to the transition between O-p states in the valence bands (VB) either to O-s states or to Mn-d states in the conduction bands (CB), and from O-p states in VB either to O-s states or to Bi-p states in CB, associated with certain energy because of the relationship between the imaginary part of the dielectric function and density of states. In spite of main peaks, there are some other peaks in the entire samples positioned at energy range from 2.0 eV to 7.0 eV, respectively, which are caused due to the direct transitions from the O-2p states to O-2s states (Fig. 4(a) and (b)). At higher energies beyond 7.0 eV, the decrease in the peaks of $\varepsilon_2^{ave}(\omega)$ is due to disalignment of the interfacial dipoles in the direction of high frequency electric field. At energy around 12.0 eV the peaks

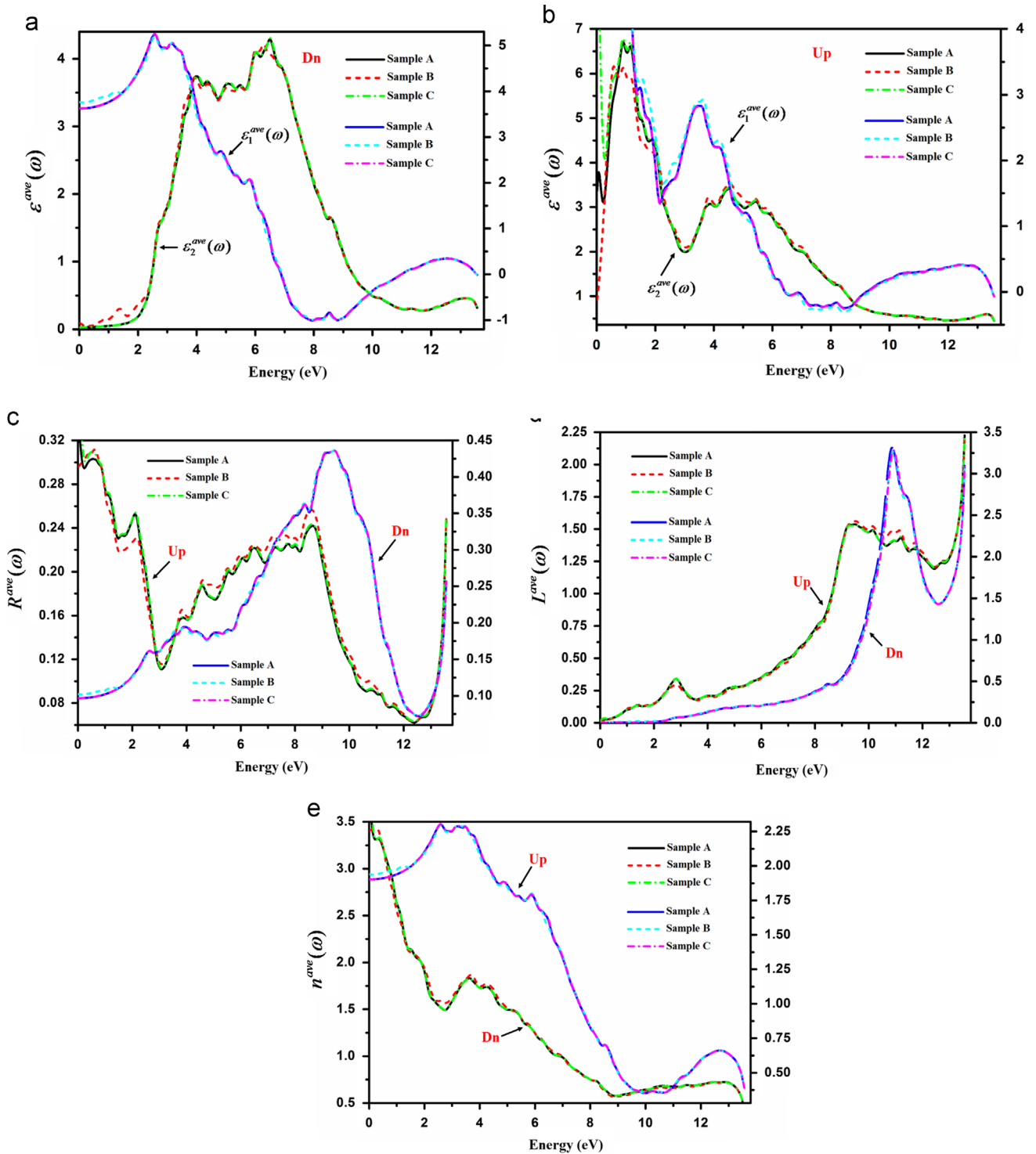


Fig. 4. Calculated real and imaginary part of dielectric function, reflectivity, energy loss function and refractive index of all samples (A, B, C), using EVGGA.

again show decline, as shown in Fig. 4(a) and (b). To the best of our knowledge, there are no experimental data or theoretical results related to the base and the location of these peaks, for meaningful comparison.

The average value of the real part $\epsilon_1^{ave}(\omega)$ of the dielectric function for the three samples (A, B and C) as a function of photon energy $\hbar\omega$ for both spin-up/dn polarization, are plotted in Fig. 4 (a) and (b). At energy ranging from 6.39 eV to 9.11 eV in spin-up and at energy from 6.87 eV to 10.85 eV in spin-dn for all three samples (A, B and C), one can notice the zero crossing of $\epsilon_1^{ave}(\omega)$,

which is associated to the position of the screened plasma frequency [32]. In this high energy range i.e. 10.85 eV, the compounds can be used as a shield for the electromagnetic radiation and these negative values correspond to the maximum values of the reflectivity. In spin-up/dn polarization, the $\epsilon_1^{ave}(\omega)$ have strong peaks at energy range from 1.74 eV to 6.66 eV, as displayed in Fig. 4(a) and (b). It is clear from Fig. 4a, the static values of the real part of the complex dielectric function are 3.62 for sample A and C, while it is 3.76 for sample B, in spin-dn polarization.

By knowing both of the imaginary and real parts of the optical dielectric function, we can calculate the refractivity $R(\omega)$, energy loss function $L(\omega)$ and refractive index $n(\omega)$. It is obvious from Fig. 4c that in the energy range from 0.0 to 13.8 eV the reflectivities $R^{ave}(\omega)$ of the three compounds show maximum peaks, which is originated from the transition between VBM to CBM except a valley appeared at 3.0 eV and beyond 12.0 eV in spin-up polarization, also a big valley is observed at 12.5 eV in spin-dn polarization. According to Reshak et al. [33], the valley of the plasmon minimum is associated to $\epsilon_2^{ave}(\omega)$ at the resonance of the plasma and typically from the degree of the overlapping between the inter-band absorption parts. Following Fig. 4c, all the samples in spin-dn polarization show high reflectivity at 9.40 eV as compared to spin-up polarization at the energy 8.60 eV, due to this high reflectivity, the compounds can also be used as Bragg's reflector in the desired energy range. The energy loss function $L^{ave}(\omega)$ is plotted in Fig. 4d. The $L^{ave}(\omega)$ spectra arise due to the energy loss of the fast moving electrons in the compounds and normally it is found large at the plasma frequency [34]. Following Fig. 4d, there are prominent peaks at energy beyond 9.0 eV (spin-up polarization) and at 11.0 eV show maximum peaks (spin-dn polarization) for sample (A and C) and for sample B, which is recognized as the plasmon peaks, that is linked to the rapid decay of the reflectance. If we look at the spectra for the $\epsilon_1^{ave}(\omega)$, which is decreasing at

higher photon energy $\hbar\omega$ that is also related efficiently to the plasmon peaks in $L^{ave}(\omega)$ for similar polarization.

The calculated average refractive index $n^{ave}(\omega)$ for the samples A, B and C are plotted in Fig. 4e. A wide spectrum of $n^{ave}(\omega)$ over energy range from 0.0 to 13.8 eV is illustrated for these compounds. Fig. 4e, shows at low energy $n^{ave}(\omega)$ has greater value, then start decline while moving towards the higher energy along the spectral region. On the other hand, all the compounds behave half metallicity, so at zero frequency, the static value of $n^{ave}(0)$ are 1.90 (sample A and C) and 1.93 (sample B), respectively. It is explained from Fig. 4e, that $n^{ave}(\omega)$ exhibit maximum value from 1.90 eV to 3.5 eV and then start decreasing at higher photon energy ($\hbar\omega$). The values of the refractive index $n^{ave}(\omega)$ show increase/decrease at certain energy ranges above 8.0 eV (spin-up) and 9.0 eV (spin-dn). It is clear from Fig. 4e that due to the variation of Bi/Mn concentration, the refractive index $n^{ave}(\omega)$ also shows variation and it decreases for sample A and C as compared to sample B at low energy along the spectral region.

3.3. Thermoelectric properties

The electronic transport properties are calculated using the Boltzmann theory employed in the BoltzTraP code [35,36], the

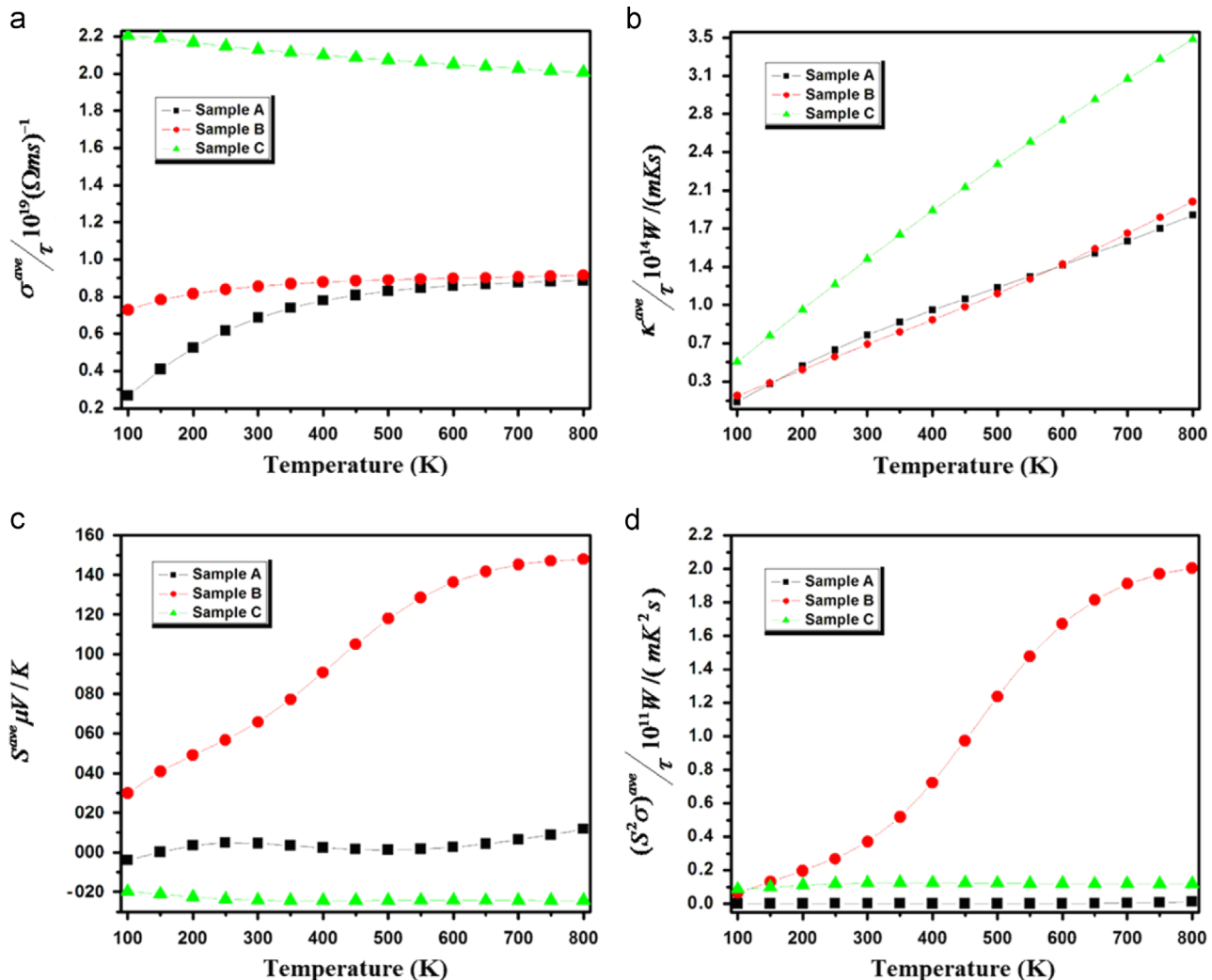


Fig. 5. Calculated transport coefficients of all samples (A, B, C), using EVGGA as a function of temperature (100–800 K): electrical conductivity, thermal conductivity, Seebeck coefficient and power factor.

expressions for the entire transport coefficients i.e. electrical conductivity, electronic thermal conductivity and Seebeck coefficient, related to the electronic structure of the materials are taken from Ref. [37].

The average value of electrical conductivity $\sigma^{ave}/\tau(T)$ for the samples (A, B and C) versus temperature, is shown in Fig. 5a. We would like to mention that, $\sigma^{ave}/\tau(T)$ of samples A and B are similar above 450 K, whereas below this temperature sample B possess greater values of electrical conductivity as compared to sample A i.e. at 100 K sample A, start from $2.5 \times 10^{19}(\Omega \text{ ms})^{-1}$ and then shows rapid increase with temperature up to 450 K, while sample B start from $7.1 \times 10^{19}(\Omega \text{ ms})^{-1}$, but it indicates gradual increases with temperature. Furthermore, the electrical conductivity of sample C behaves differently with temperature as compared to samples A and B, it shows decline in the electrical conductivity value with increasing the temperature due to the scattering of phonon.

The temperature dependent average value of the electronic thermal conductivity $\kappa^{ave}/\tau(T)$ for the three samples (A, B, and C), are summarized in Fig. 5b. Sample C depicts quite bigger value of the average value of electronic thermal conductivity as compared to samples A and B, which has approximately the same behavior like increasing trend with temperature, for different concentration of Bi/Mn in all samples. Initially at 100 K, the thermal conductivity for the entire samples exhibit lower values due to electrons-phonon scattering (by different Bi/Mn concentration), vacancies or other fixed defects, which in practically, result unimaginative dependence of temperature. In order to discuss the main scattering phenomenon, the total average thermal conductivity is divided into two parts: one from the electron contribution and second from the lattice contribution, but here we ignore the lattice thermal conductivity. It is clear from Fig. 5b that all samples (A, B and C) exhibit a linear increase with temperature and gain its maximum values i.e. $1.5 \times 10^{14} \text{ W}/(\text{mK s})$ (sample A), $2.1 \times 10^{14} \text{ W}/(\text{mK s})$ (sample B) and $4.9 \times 10^{14} \text{ W}/(\text{mK s})$ (sample C) at 800 K. According to Callaway model [38], which give explanation in detail and permits us to consider the thermal conductivity of phonons, that account the individual scattering process by suitable relaxation times that is $\tau_c : \tau_c^{-1} = \tau_B^{-1} + \tau_D^{-1} + \tau_e^{-1} + \tau_U^{-1}$, where the indices B, D, e and U denote the phonon scattering caused by the crystal boundaries, defects, electrons and Umklapp process, respectively. At higher temperatures, the Umklapp process is a powerful scattering phenomena to enhance the average value of thermal conductivity of electrons (Fig. 5b) [39,40]. Following Fig. 5b, at higher temperature (800 K), the sample C has greater $\kappa^{ave}/\tau(T)$ as compared to samples A and B.

Fig. 5c displays the temperature dependent average Seebeck coefficient $S^{ave}(T)$ for the three samples (A, B and C), for different Bi/Mn concentrations. One can see from Fig. 5c that the sample C reveal negative Seebeck coefficient $S^{ave}(T)$ along the entire range of temperature from 100 K to 800 K, which indicate electrons-doped material, that is used as the main charge carriers in this sample. The average value of the Seebeck co-efficient of sample A possess fluctuation around zero and then shows increase positively at higher temperature, beyond 650 K (Fig. 5c). In Fig. 5c, sample B shows large and positive value ($30 \mu\text{V}/\text{K}$) of Seebeck coefficient at low temperature and increases exponentially up to 650 K. Above 650 K, sample B shows stability (saturation) and sample C reaches its minimum value. Consequently, sample B presents majority holes transport as compared to other two samples indicate large value of the average Seebeck co-efficient (Fig. 5c), which takes place due to the depletion of charge carriers in sample B. We use the Mott's formula [41],

$$S_d(T)\theta_D = \frac{\pi^2 k_B^2 2m}{e\hbar^2 (3n\pi^2)^{2/3}} T$$

where m = mass of the carriers, and e = the charge of the carriers, which permits to derive the charge carrier density n . It is acknowledged that the above equation is legitimate for systems with no important electronic correlations.

It is cleared from the Mott's formula that the Seebeck coefficient depends on the carrier concentration, effective mass and temperature. The Mott's formula explain the hopping mechanism of electrons occur between the localized states to the minimum of the conduction band [42,43] and also explain exactly the interaction between independent electrons and static impurities.

In thermoelectric properties, the power factor is an important part, which influences directly the thermoelectric performance. The average of power factor $S^{ave2}\sigma/\tau(T)$ as a function of temperature is shown in Fig. 5d. Fig. 5d, shows that both samples A and C show the same behavior power factor $S^{ave2}\sigma/\tau(T)$ throughout the entire temperature range from 100 K to 800 K, respectively. $S^{ave2}\sigma/\tau(T)$ of sample B is $0.6 \times 10^{11} (\Omega \text{ ms})^{-1}$ at 100 K and then increases with temperature, reaches its maximum value $2 \times 10^{11} (\Omega \text{ ms})^{-1}$ at 800 K [44]. One can note from the Fig. 5d, that the compound (sample B), which has greater hole concentration is more useful for thermoelectric materials as compared to the sample A and C.

4. Conclusion

Density functional theory is used to carry out the calculations to examine the structural and magnetic properties of three samples, we call them as A, B and C. Our calculations prove that the entire samples (A, B and C) depict half-metallicity. Our calculations specify that these samples illustrate high spin polarization at Fermi level, which is mainly contributed by the Mn-3d orbital electrons. Our calculated results specify that the total magnetic moment of the three samples is due to Mn atom. The spin oriented optical properties are calculated and analyzed, which show that the sample B as compared to samples A and C can be used as optoelectronic devices, due to the higher response in the UV and visible region of spectrum. We also have calculated the thermoelectric properties as a function of temperature, from which we concluded that the sample B is more useful for thermoelectric materials than sample A and C.

Acknowledgement

This result was developed within the CENTEM project, reg. no. CZ.1.05/2.1.00/03.0088, co-funded by the ERDF as part of the Ministry of Education, Youth and Sports OP RDI program. Meta-Centrum and the CERIT-SC under the program Centre CERIT Scientific Cloud, reg. no. CZ.1.05/3.2.00/08.0144.

References

- [1] Y. Tokura, S. Seki, Adv. Mater. 22 (2010) 1554.
- [2] R.M. Kenzelmann, A.B. Harris, S. Jonas, C. Broholm, J. Schefer, S.B. Kim, C.L. Zhang, S.W. Cheong, O.P. Vajk, J.W. Lynn, Phys. Rev. Lett. 95 (2005) 087206.
- [3] N. Ikeda, H. Ohsumi, K. Ohwada, K. Ishii, T. Inami, K. Kakurai, Y. Murakami, K. Yoshii, S. Mori, Y. Horibe, H. Kitō, Nature 436 (2005) 1136.
- [4] N. Hur, S. Park, P.A. Sharma, J. Ahn, S. Guha, S.W. Cheong, Nature 429 (2004) 392.
- [5] S. Quezel-Ambrunaz, E.F. Bertaut, G.C.R. Buisson, Acad. Sci. 258 (1964) 3025.
- [6] E.F. Bertaut, G. Buisson, A. Durif, A. Mareschal, M.C. Montmory, S. Quezel-Ambrunaz, Bull. Soc. Chim. Fr. (1965) 1132.
- [7] J.A. Alonso, M.T. Casais, M.J. Martínez-Lope, I. Rasines, J. Solid State Chem. 129 (1997) 105.
- [8] M. Retuerto, M.J. Martínez-Lope, K. Krezhov, M.T. Fernández-Díaz, J.A. Alonso, J. Solid State Chem. 184 (2011) 2428.
- [9] A. Muñoz, J.A. Alonso, M.J. Martínez-Lope, J.L. Martínez, Chem. Mater. 16 (2004) 4087.
- [10] D.M. Gaiquinta, H.C. zur Loye, J. Alloys Compd. 184 (1992) 151.

- [11] N. Nguyen, M. Legrain, A. Ducouret, B. Raveau, J. Mater. Chem. 9 (1999) 73.
- [12] A. Munoz, J.A. Alonso, M.T. Casais, M.J. Martinez-Lope, J.L. Martinez, M.T. Fernandez-Diaz, Phys. Rev. B: Condens. Matter 65 (2002) 144423.
- [13] R.J. Jia, J.T. Han, X.J. Wu, C.L. Wu, Y.H. Huang, W. Huang, Mater. Res. Bull. 43 (2008) 1702.
- [14] K. Saravana Kumar, C. Venkateswaran, J. Phys. D: Appl. Phys. 44 (2011) 3250001.
- [15] Y.Q. Lin, Y.J. Wu, X.M. Chen, S.P. Gu, J. Tong, S. Guan, J. Appl. Phys. 105 (2009) 054109.
- [16] I. Fier, L. Walmsley, A. Souza, J. Appl. Phys. 110 (2001) 084101.
- [17] Q. Liu, D. Sallagoity, M. Josse, O. Toulemonde, Inorg. Chem. 52 (2013) 7853–7861.
- [18] J.M. Ziman, Principles of the Theory of Solids, Cambridge University Press, Cambridge, U.K, 1964.
- [19] P.B. Allen, in: J.R. Chelikowsky, S.G. Louie (Eds.), Quantum Theory of Real Materials, Kluwer, Boston, 1996, pp. 219–250.
- [20] P. Balaha, K. Shewartz, G.K.H. Madsen, D. Kvsnicka, J. Luitz, WIEN2K, an Augmented Plane Wave +local Orbitals Program for Calculating Crystals Properties, Karlheinz Schewartz, Techn. Universitat, Wien, Austria, ISBN 3-9501031-1-2, 2001.
- [21] D.M. Ceperley, B.I. Alder, Phys. Rev. Lett. 45 (1980) 566–569.
- [22] J.P. Perdew, K. Burke, M. Ernzerhof, Phys. Rev. Lett. 77 (1996) 3865–3868.
- [23] E. Engel, S.H. Vosko, Phys. Rev. B: Condens. Matter. 47 (1993) 13164–13174.
- [24] C.D. Brunetta, B. Karuppanan, K.A. Rosmus, J.A. Aitken, J. Alloys Compd. 516 (2012) 65–72.
- [25] A.H. Reshak, S.A. Khan, H. Kamarudin, Jiri Bila, J. Alloys Compd. 582 (2014) 6–11.
- [26] Y.X. Wang, W.L. Zhong, C.L. Wang, P.L. Zhang, Solid State Commun 120 (2001) 137–140.
- [27] H.S. Saini, M. Singh, A.H. Reshak, M.K. Kashyap, Comput. Mater. Sci. 74 (2013) 114–118.
- [28] T.P. Kaloni, S. Gangopadhyay, N. Singh, B. Jones, U. Schwingenschlög, Phys. Rev. B: Condens. Matter 88 (2013) 235418.
- [29] T.G. Pedersen, P. Modak, K. Pedersen, N.E. Christensen, M.M. Kjeldsen, A.N. Larsen, J. Phys. Condens. Matter 21 (2009) 115502–115507.
- [30] N. Singh, T.P. Kaloni, Udo Schwingenschlög, Appl. Phys. Lett. 102 (2013) 023101.
- [31] A.H. Reshak, H. Kamarudin, S. Auluck, J. Mater. Sci. 48 (2013) 1955–1965.
- [32] B. Amin, Iftikhar Ahmad, M. Maqbool, S. Goumri-Said, R. Ahmad, J. Appl. Phys. 109 (2011) 023109.
- [33] A.H. Reshak, et al., J. Magn. Magn. Mater. 324 (2012) 1397–1405.
- [34] P. Nozieres, Phys. Rev. Lett. 8 (1959) 1.
- [35] G.K.H. Madsen, D.J. Singh, Comput. Phys. Commun. 175 (2006) 67.
- [36] G.K.H. Madsen, J. Am. Chem. Soc. 128 (2006) 12140.
- [37] J.C. Zheng, Front. Phys. Chin 3 (2008) 269.
- [38] J. Callaway, H.C. von Baeyer, Phys. Rev. 120 (1969) 1149.
- [39] P. Rogl, et al., Acta Mater. 59 (2011) 2368–2384.
- [40] B. Amin, N. Singh, T.M. Tritt, H.N. Alshareef, U. Schwingenschlög, Appl. Phys. Lett. 103 (2013) 031907.
- [41] F.J. Blatt, Physics of Electronic Conduction in Solids, McGraw-Hill, New York (1968) 210.
- [42] A. Skumamch, A. Frova, N.M., Am. Solid State Commun 54 (1985) 597.
- [43] B. Abay, H.S. Guder, H. Efeoglyu, Y.K. Yogyurtcu, Physica B 254 (1998) 148.
- [44] R.Z. Zhang, X.Y. Hua, P. Guo, C.L. Wang, Physica B 407 (2012) 1114–1118.